applied sciences

MDPI

Article

How the Rigid and Deformable Image Registration Approaches Affect the Absorbed Dose Estimation Using Images Collected before and after Transarterial Radioembolization with ^{90}Y Resin Microspheres in a Clinical Setting

Giuseppe Della Gala [1,†], Miriam Santoro [1,2,†], Giulia Paolani [1,2,*], Silvia Strolin [1], Alberta Cappelli [3], Cristina Mosconi [3], Elisa Lodi Rizzini [4] and Lidia Strigari [1,*]

[1] Department of Medical Physics, IRCCS Azienda Ospedaliero-Universitaria di Bologna, 40138 Bologna, Italy
[2] Medical Physics Specialization School, Alma Mater Studiorum, University of Bologna, 40138 Bologna, Italy
[3] Department of Radiology, IRCCS Azienda Ospedaliero-Universitaria di Bologna, 40138 Bologna, Italy
[4] Radiation Oncology, IRCCS Azienda Ospedaliero-Universitaria di Bologna, 40138 Bologna, Italy
* Correspondence: giulia.paolani@aosp.bo.it (G.P.); lidia.strigari@aosp.bo.it (L.S.)
† These authors contributed equally to work.

Abstract: Background: Transarterial radioembolization (TARE) relies on directly injected ^{90}Y- or ^{166}Ho-loaded microspheres in the hepatic arteries. The activity to be injected is generally based on pre-TARE ^{99m}Tc-macro-aggregated-albumin (MAA) imaging, while the actual dose distribution is based on post-treatment images. The volume of interest (VOIs) propagation methods (i.e., rigid and deformable) from pre- to post-TARE imaging might affect the estimation of the mean absorbed dose in the tumor and non-tumoral liver (NTL), i.e., D_T and D_{NTL}, respectively. Methods: In 101 consecutive patients, liver and tumor were delineated on pre-TARE images and semi-automatically transferred on ^{90}Y-PET/CT images with a rigid or deformable registration approach. Pre- and post-TARE volumes and $D_T/D_{NTL}/D_L$ were compared using correlation coefficient (CC) indexes, such as intra-class (ICC), Pearson's (PCC), concordance (CCCo) and Bland–Altman analyses. The Kaplan–Meier curves of overall survival (OS) were calculated according to D_T. Results: All computed CCs indicated very good (>0.92) agreement for volume comparison, while they suggested good (ICC $\geq$ 0.869, PCC $\geq$ 0.876 and CCCo $\geq$ 0.790) and moderate agreement in the intra- and inter-modality $D_T/D_{NTL}/D_L$ comparisons, respectively. Bland–Altman analyses showed percentage differences between the manual and deformable approaches of up to about −31%, 9% and 62% for tumoral volumes, D_T and D_{NTL}, respectively. The overall survival analysis showed statistically significant differences using D_T cutoffs of 110, 90 and 85 Gy for the manual, rigid and deformable approaches, respectively. Conclusions: The semi-automatic transfer of VOIs from pre- and post-TARE imaging is feasible, but the selected method might affect prognostic D_T/D_{NTL} constraints.

Keywords: transarterial radioembolization; dosimetry; image registration; delineation

Citation: Della Gala, G.; Santoro, M.; Paolani, G.; Strolin, S.; Cappelli, A.; Mosconi, C.; Lodi Rizzini, E.; Strigari, L. How the Rigid and Deformable Image Registration Approaches Affect the Absorbed Dose Estimation Using Images Collected before and after Transarterial Radioembolization with ^{90}Y Resin Microspheres in a Clinical Setting. *Appl. Sci.* **2022**, *12*, 12767. https://doi.org/10.3390/app122412767

Academic Editors: Ioanna Kyriakou and Chang Ming Charlie Ma

Received: 12 September 2022
Accepted: 1 December 2022
Published: 12 December 2022

1. Introduction

Transarterial radioembolization (TARE) is one the most effective treatments for unresectable primary and secondary hepatic lesions. In TARE, ^{90}Y-loaded resin (SIR-Spheres®, Sirtex Medical Ltd., Woburn, MA, USA) or glass (TheraSphere™, Boston Scientific, Marlborough, MA, USA) microspheres or ^{166}Ho-loaded PLLA microspheres (Quiremspheres®, Quirem Medical B.V. subsidiary of Terumo Corporation, Tokyo, Japan)) are selectively injected in the hepatic arteries. The injection leads to a preferential deposition in the tumoral tissues, hence sparing the healthy liver lobes.

The use of ^{99m}Tc-macro aggregated albumin (^{99m}Tc-MAA) SPECT/CT for treatment planning to assess the target coverage is largely established and recommended in the

operating instructions of these devices as well as in the international recommendations [1–3]. Moreover, the ^{99m}Tc-MAA SPECT/CT images are mandatory to evaluate the possible extrahepatic shunts [4] or to identify patients with a Lung Shunt Fraction (LSF) > 20%, both representing exclusion criteria for TARE patients. More recently, exclusively for ^{166}Ho-based TARE treatment, ^{99m}Tc-MAA images have been replaced by ^{166}Ho-Scout dose (using an activity up to 250 MBq) to accurately predict the activity distribution of the therapeutic injection of ^{166}Ho-loaded microspheres [5]. Nevertheless, ^{99m}Tc-MAA imaging remains the state-of-the-art approach for predicting the therapeutic ^{90}Y-loaded TARE activity distribution.

Specifically, pre-treatment ^{99m}Tc-MAA SPECT/CT 3D voxel-based dosimetry allows the calculation of the absorbed dose distribution expected in patients after the TARE procedure, which can be used to identify the ^{90}Y activity to be administered in order to increase the tumor control while reducing the possible risk of toxicity. In addition, the post-treatment ^{90}Y PET/CT-image-based dosimetry allows the verification of the planned absorbed dose distribution.

Pre-treatment voxel-based dosimetry requires the importing of DICOM images, delineation of volumes of interest (VOIs), calculation of the absorbed dose distribution and computing and evaluation of the dose volume histograms (DVHs). These operations can be performed using CE or FDA marked treatment planning systems (TPSs) [6]. In particular, regarding the operation of VOI contouring, nuclear medicine or interventional radiologist physicians can manually or semi-automatically delineate the tumor, lungs, whole liver and non-tumoral liver (NTL) on SPECT/CT images.

Moreover, the available images for TARE generally also include contrast-enhanced computed tomography (CECT) and ^{90}Y PET/CT images. In each of these modalities, all the VOIs might be manually delineated to obtain target volumes or to perform post-treatment dosimetry. Alternatively, deformable or rigid image registration algorithms are implemented in commercial TPSs to transfer VOIs from any reference modality (e.g., ^{99m}Tc-MAA SPECT/CT) to another (e.g., ^{90}Y PET/CT) [6].

Unfortunately, the manual delineation of VOIs is time-consuming and might affect the accuracy of the volume, shape and position of the target and organs at risk (OARs), due to the inter-operator delineation variability on a given image [7]. This has been previously shown in TARE, where the variability between different readers led to tumor-absorbed doses with a low intra-class correlation coefficient (ICC), while showing higher ICC values for liver-absorbed doses [8]. In addition, other sources of VOI delineation discrepancies among image modalities are due to respiratory motion and liver deformation [9].

Several authors investigated the impact of the dose calculation method (e.g., dose kernel convolution vs. local deposition) on absorbed dose distributions [10–13] and the agreement between pre- and post-treatment image-based dosimetry [14–18]. However, the impact of different VOI propagation modalities demands additional investigations.

In this study, the impact of deformable or rigid registration algorithms implemented in a commercial TPS was assessed in terms of the agreement of volumes and mean absorbed doses on post-treatment dosimetry images and compared to ones calculated using pre-treatment images.

In addition, the correlation between overall survival and tumor mean absorbed doses extracted from pre- and post-treatment dosimetry based on deformable or rigid registration was assessed on a large cohort of TARE patients.

2. Materials and Methods

2.1. Planning and Verification Dosimetry Workflows

In the following sections, the protocol adopted for patient selection, planning and treatment verification is reported and comprehensively summarized in Figure 1. All patients included in the study followed the described protocol.

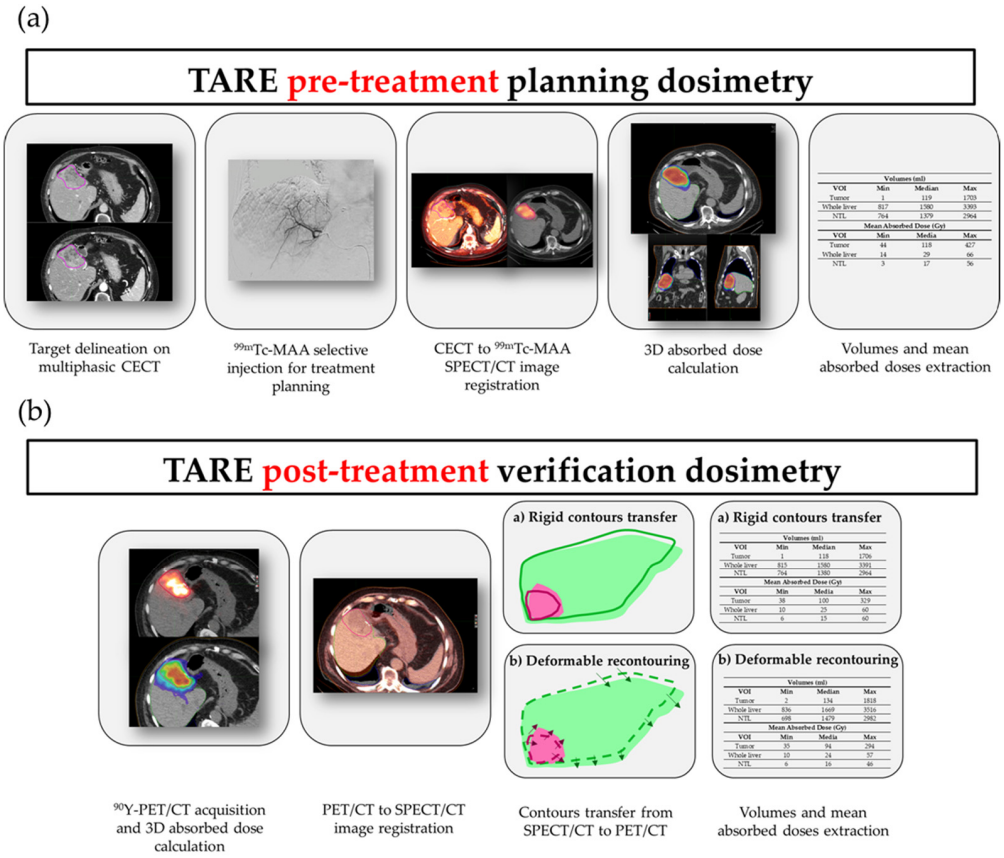

Figure 1. TARE pre-treatment planning dosimetry (panel (**a**)) and post-treatment verification dosimetry (panel (**b**)) workflows.

2.1.1. Patient Eligibility for TARE Treatment

The eligibility of patients was discussed by a multidisciplinary team that included professionals of Interventional Radiology, Radiation Oncology, Nuclear Medicine, Hepatology, Surgery and Medical Physics. Inclusion criteria included: age >18 years, unresectable primary or secondary liver disease. Exclusion criteria included: presence of extrahepatic metastasis; reduced liver functionality; strong impairment of blood tests (bilirubin, albumin); LSF > 20%.

2.1.2. Pre-Treatment Images and Angiographic Procedure

When considered eligible for the treatment, patients underwent a multiphasic CECT to properly identify the intrahepatic tumoral or metastatic areas. The CECT was acquired within one to three weeks from planning the angiographic procedure. The manual contouring of the tumor was jointly performed by the Radiation Oncology and the Interventional Radiology physicians using MIM SurePlan Liver Y90 (MIM Software Inc., Cleveland, OH, USA) by reviewing the arterial or venous phases of the CECT. In a limited number of cases, a magnetic resonance acquisition with contrast media was used for target delineation instead of the CECT.

An angiographic procedure was fully performed to correctly identify the hepatic arteries that primarily supplied the tumor, as described by Gramenzi et al. [19]. During the angiographic procedure, a 150 MBq injection of ^{99m}Tc-MAA was performed.

2.1.3. SPECT/CT Imaging

After the angiographic procedure, SPECT/CT and a planar scintigraphy were acquired within one hour.

Planar scintigraphy and SPECT/CT were acquired on a dual-head Discovery 670 NM/CT (GE Healthcare, Chicago, IL, USA; Milwaukee, Brookfield, WI, USA) equipped with low-energy high-resolution collimators, 60 views, 2 projections-per-view and 15 s of acquisition per frame. Ordered subset expectation maximization (OSEM) reconstruction algorithm (2 iterations, 10 subsets, Butterworth post-filtering with order 10 and cutoff frequency 0.48) was used. Attenuation correction based on hybrid CT image, scatter correction (energy window: 120 ± 5 keV) and resolution recovery was applied.

The LSF was assessed on planar scintigraphy. If an LSF > 20% was measured or unwanted/unavoidable shunts to other districts (e.g., gastric shunt) occurred, the patient was excluded from the treatment.

2.1.4. Pre-Treatment Dosimetry and Activity Determination

The phase of the CECT selected for the contouring was rigidly registered to the CT of the SPECT/CT acquisition and the delineated target volume was transferred from the CECT to the SPECT/CT image. Organs at risk (i.e., liver and lungs) were delineated on the CT of the SPECT/CT acquisition using manual contouring or semi-automated tools provided by the TPS. Non-tumoral liver was obtained as a boolean subtraction of the target contour from the whole liver contour.

Activity prescription was performed according to MIRD equations by partitioning the liver and the lungs [20]. The activity was prescribed so that not exceeding 40 Gy to the whole liver. For hepatocellular carcinoma (HCC) patients included in a research trial comparing personalized voxel-based activity prescription with body surface area (BSA) or MIRD activity prescription methods (clinicaltrial.gov ID: NCT05227482), the activity was prescribed based on voxel-based dosimetry obtained on SPECT/CT images to achieve a tumor mean absorbed dose of at least 150 Gy while not exceeding 40 Gy to the normal liver.

2.1.5. Post-Treatment Residual Activity Assessment

All treatments were performed within one to three weeks from the planning ^{99m}Tc-MAA injection. All patients were treated in an angiographic procedure that replicated the arterial access employed during the planning injection. Residual activity in the catheters or in the vial were evaluated after the treatment in an experimental setup by multiple acquisitions at fixed distance with an ionization chamber [21].

2.1.6. PET/CT Imaging

All patients received a ^{90}Y PET/CT acquisition the day after the treatment (typically about 20 h after the ^{90}Y administration).

The PET/CT images were acquired on a Discovery MI (GE Healthcare, Chicago, IL, USA; Milwaukee, Brookfield, WI, USA) 3-rings system with time-of-flight (TOF) corrections. Time-of-flight and attenuation correction based on hybrid CT image was always applied. The acquisition protocol consisted of three beds per patient, 10 min per bed.

The image reconstruction system was equipped with a Bayesian penalized likelihood reconstruction algorithm named Q.Clear [22]. The Q.Clear algorithm had a noise suppression term controlled by a parameter, indicated as β, which was the only user-input variable to the algorithm [23]. In this study, a β-value of 4000 was adopted for PET/CT image reconstruction as reported by Hou et al. [24].

2.2. Voxel-Based Dosimetry Tools

Pre-treatment voxel-based dosimetry was performed on pre-treatment ^{99m}Tc-MAA SPECT/CT acquisitions with MIM SurePlan Liver Y90. For dose calculation purposes, all counts of the SPECT acquisition in the field-of-view (FOV) were considered and normalized to an injected activity of 1 GBq ("With known activity" approach). When the pre-treatment dosimetry was used for activity planning, the 1 GBq injected activity was eventually scaled by the user to obtain the desired dose to the target and/or OARs. The dose distributions were obtained with a local deposition method (LDM) [11], which assumed a liver-like

density over the entire FOV. After the TARE procedure, the pre-treatment dose distribution was scaled to the actual injected ^{90}Y activity and used for the subsequent comparison.

Post-treatment voxel-based dosimetry was obtained from the post-treatment PET/CT acquisition, with the same LDM, based on the total injected activity in the FOV.

Of note, the CE market workflow implemented in MIM for the post-treatment dosimetry is based on the deformable propagation of VOIs, while the rigid propagation can be implemented by the user. Thus, we decided to focus the study on these two methods.

In more detail, the deformable registration algorithm, which allowed for volume adaptation using the CT images based on Hounsfield units (HU) [25], was applied as default of the workflow named "LDM with known activity". In addition, the contours of the target and OARs were rigidly transferred from the SPECT/CT to PET/CT images, maintaining the structure volumes, using the "Box-based" image registration MIM tool. This box was manually placed to include the tumor and its surrounding organs or tissues (i.e., structures with different electronic densities or HU), facilitating the relocation of the target when liver modifications occurred from one image modality to the other.

2.3. Patients

The investigated cohort included liver cancer patients who underwent TARE with ^{90}Y resin microspheres at our Institute from April 2017 with a minimum follow up of 3 months, for whom VOIs obtained from both deformable and rigid image registration algorithm were available. The written consensus was obtained for patients enrolled in the prospective clinical trial (clinicaltrial.gov ID: NCT05227482), while for the remaining ones ethics approval and participant consent were not necessary as this study involved the use of retrospective de-identified data according to "Determinazione AIFA-20 Marzo 2008 (G.U. n. 76, 31-03-2008)".

2.4. Volumes and Mean Absorbed Dose Comparisons and Statistical Analysis

The volumes were separately obtained according to pre- and post-treatment images and the adopted modality for VOI generation (i.e., manual contouring on pre-treatment images, termed as $V_{T,m}$, $V_{L,m}$ and $V_{NTL,m}$ for tumor, liver and NTL, respectively, and rigid or deformable registration algorithms on post-treatment images, named $V_{T,r}$, $V_{L,r}$, $V_{NTL,r}$ and $V_{T,d}$, $V_{L,d}$, $V_{NTL,d}$, respectively). Mean absorbed doses by the tumor, the liver and the NTL were determined from the pre-treatment and the post-treatment absorbed dose distributions accordingly. In particular, on the same post-treatment absorbed dose distribution, mean absorbed doses were separately extracted for the rigid and deformable recontouring workflow. These will be referred to as $D_{T,m}$, $D_{T,r}$ and $D_{T,d}$ for tumor, $D_{NTL,m}$, $D_{NTL,r}$ and $D_{NTL,d}$ for NTL and $D_{L,m}$, $D_{L,r}$ and $D_{L,d}$ for liver.

For all volumes and absorbed mean doses, the comparisons between the pre-treatment and post-treatment data (separately for rigid and deformable recontouring approach) and between rigid and deformable recontouring method on the same post-treatment absorbed dose distribution were performed following a Bland–Altman analysis. In this analysis, the average difference between the two measurements represented the bias, while the 95% limits of agreement (LOA), obtained by the bias $\pm$ the standard deviation multiplied by 1.96, represented the precision. Agreement was also assessed by the ICC, the Pearson's correlation coefficient and the concordance correlation coefficient (CCCo); a value ≥ 0.8 indicated excellent correlation. Statistical significance was defined by a p-value < 0.05.

2.5. Survival Analysis

The Kaplan–Meier (K–M) curves of overall survival (OS) were determined from the date of the TARE procedure to the last available follow up. The K–M curves were stratified according to tumor type and tumor mean absorbed doses, determined using $V_{T,m}$, $V_{T,r}$ and $V_{T,d}$.

For each dose dataset (i.e., manual and rigid or manual and deformable) of HCC, CCC and mixed HCC/CCC patients, a tumor mean absorbed dose cutoff was obtained to split survival curve. These dosimetric cutoffs were calculated by iterating the calculation of K–M curves among a range of possible dose cutoff values and keeping the highest dose cutoff resulting in p-value < 0.05 between balanced populations (i.e., assuming a splitting between 40% and 60% of the study population).

The confusion matrixes were calculated reporting the number of doses higher or lower than the cutoff estimated for each VOI delineation/propagation approach.

All the analyses were performed using the statistical language R v.4.0.2 (https://www.r-project.org/ (accessed on 30 November 2022)) and the software RStudio v.1.2.1335 (R Core Team, Vienna, Austria).

3. Results

3.1. Patient Cohort

A total of 101 patients (58 males, 43 females) were analyzed. Median age at treatment was 68.5 years (min: 38.1 y, max: 96.7 y). Among them, 75 patients had a diagnosis of HCC, 14 cholangiocarcinoma (CCC) or mixed HCC/CCC and 12 liver metastases of various primary tumors. Portal vein thrombosis was reported in 60 out of 101 patients.

Treated tumor and whole liver volumes are reported in Table 1. Median (range) prescribed activity was 1.2 GBq (0.4; 3.5).

Table 1. Volumes of treated tumor and whole liver in mL.

VOI	Min Volume (mL)	Median Volume (mL)	Max Volume (mL)
Treated tumor	1.3	118.5	1702.9
Whole liver	816.8	1580.2	3393.3
NTL	764.2	1379.3	2964.1

The median (range) follow up was 424 days (90; 1863).

3.2. Impact of Rigid and Deformable Image Registration Algorithms on VOI Volumes

Figure 2 shows the Bland–Altman analyses between V_m, V_r and V_d for liver, tumor and NTL. The largest absolute bias was observed between $V_{L,m}$ and $V_{L,d}$ (−103.4 mL), while the largest relative bias was found between $V_{T,m}$ and $V_{T,d}$ (−30.8%). All absolute and relative biases and LOAs are reported in Supplementary Materials (Tables S1 and S2, respectively).

The correlation coefficient (CC) indexes, such as intra-class (ICC), Pearson's (PCC), concordance (CCCo) of volumes for target, liver and NTL are reported in Table 2. All CC indexes were >0.995 for volume comparison between V_m and V_r. The deformable registration approach always presented CC indexes > 0.92. All the investigated datasets were statistically significant ($p < 0.001$).

3.3. Impact of Rigid and Deformable Image Registration Algorithms on Mean Absorbed Doses

In Figure 3, panels (a,c,e), respectively, the Bland–Altman analyses between $D_{T,m}$ and $D_{T,r}$, between $D_{T,m}$ and $D_{T,d}$ and between $D_{T,r}$ and $D_{T,d}$ are reported. The largest absolute bias was observed between $D_{T,m}$ and $D_{T,d}$ (−41.7 Gy). For this comparison, the 95% LOA was −70.1 and +153.5 Gy. Bias and positive (LOA+) and negative (LOA−) LOAs are reported in Supplementary Materials (Table S1 for absolute values and Table S2 for percentage values) for all the investigated dose comparisons.

The CC indexes of mean absorbed doses for target, liver and NTL are reported in Table 2. All these indexes were statistically significant ($p < 0.001$).

A good correlation was found for the intra-modality comparisons of the mean absorbed doses (i.e., D_r and D_d) for all the investigated VOIs (i.e., ICC $\geq$ 0.869, PCC $\geq$ 0.876 and CCCo $\geq$ 0.790). Moderate correlation was found for inter-modality comparisons (i.e., D_m and D_r or D_m and D_d), as reported in Table 2.

The CCCo among tumor mean absorbed doses (i.e., $D_{T,m}$ vs. $D_{T,r}$, $D_{T,m}$ vs. $D_{T,d}$ and $D_{T,r}$ vs. $D_{T,d}$) were 0.602 (0.479; 0.701), 0.493 (0.368; 0.601) and 0.904 (0.856; 0.936) for HCC/CCC patients, while they were 0.579 (0.101; 0.840), 0.512 (0.065; 0.788) and 0.967 (0.913; 0.988) for metastatic patients.

In Figure 2, panels (b,d,f), respectively, the Bland–Altman analyses between $D_{NTL,m}$ and $D_{NTL,r}$, between $D_{NTL,m}$ and $D_{NTL,d}$ and between $D_{NTL,r}$ and $D_{NTL,d}$ are reported. The largest absolute bias was observed between $D_{NTL,m}$ and $D_{NTL,d}$ (−2.3 Gy).

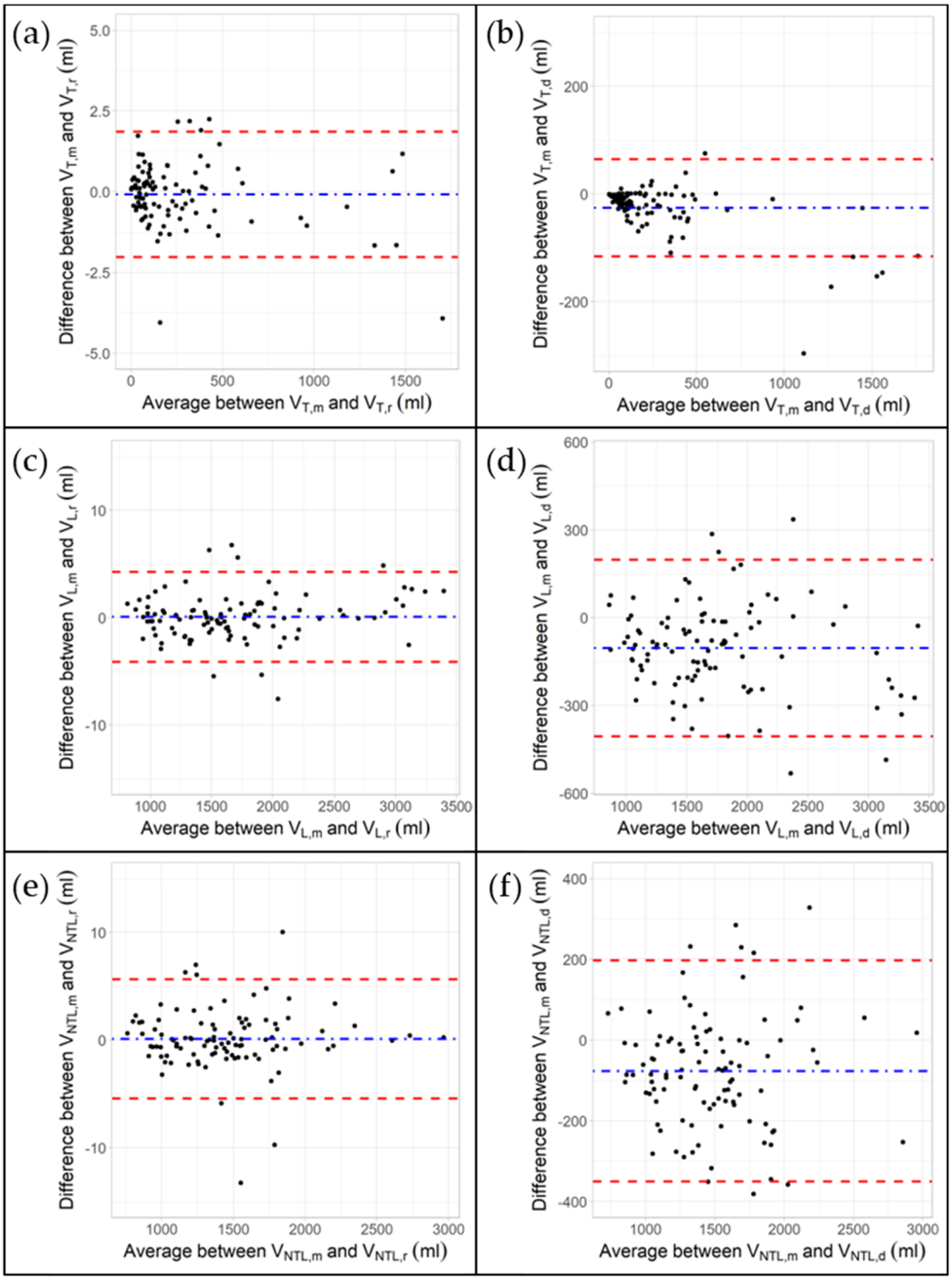

Figure 2. Bland–Altman plots for tumor (i.e., panels (**a**,**b**)), whole liver (i.e., panels (**c**,**d**)) and NTL (i.e., panels (**e**,**f**)) volumes according to the contouring approach.

Table 2. ICC of volumes and mean absorbed doses vs. the methods of VOI delineation and propagation. Ninety-five percent confidence intervals (CI) of CCCo are reported. § All values were statistically significant ($p < 0.001$).

Var.1	Var.2	ICC §	Pearson §	CCCo (95% CI)
$D_{T,r}$	$D_{T,d}$.	0.875	0.908	0.875 (0.826; 0.911)
$D_{T,m}$	$D_{T,r}$	0.590	0.707	0.605 (0.491; 0.699)
$D_{T,m}$	$D_{T,d}$	0.486	0.721	0.524 (0.418; 0.617)
$V_{T,r}$	$V_{T,d}$	0.990	0.995	0.990 (0.986; 0.993)
$V_{T,m}$	$V_{T,r}$	1.000	1.000	1.000 (1.000; 1.000)
$V_{T,m}$	$V_{T,d}$	0.990	0.995	0.990 (0.986; 0.992)
$D_{NTL,r}$	$D_{NTL,d}$.	0.869	0.876	0.790 (0.713; 0.846)
$D_{NTL,m}$	$D_{NTL,r}$	0.820	0.843	0.821 (0.748; 0.873)
$D_{NTL,m}$	$D_{NTL,d}$	0.787	0.842	0.789 (0.713; 0.846)
$V_{NTL,r}$	$V_{NTL,d}$	0.927	0.940	0.927 (0.894; 0.950)
$V_{NTL,m}$	$V_{NTL,r}$	0.996	0.996	0.996 (0.994; 0.997)
$V_{NTL,m}$	$V_{NTL,d}$	0.929	0.944	0.929 (0.897; 0.951)
$D_{L,r}$	$D_{L,d}$.	0.930	0.931	0.929 (0.897; 0.952)
$D_{L,m}$	$D_{L,r}$	0.860	0.907	0.862 (0.807; 0.903)
$D_{L,m}$	$D_{L,d}$	0.859	0.925	0.863 (0.810; 0.902)
$V_{L,r}$	$V_{L,d}$	0.959	0.971	0.959 (0.941; 0.972)
$V_{L,m}$	$V_{L,r}$	0.998	0.998	0.998 (0.997; 0.999)
$V_{L,m}$	$V_{L,d}$	0.957	0.971	0.957 (0.938–0.971)

The difference between the predicted and the observed doses of NTL was lower than 12 Gy, suggested in Jadoul et al. [17], in 96 out of 101 patients (deformable contouring approach) and 97 out of 101 patients (rigid contouring approach). In the remaining five of the deformable contouring group, the pre-treatment NTL mean absorbed dose always overestimated the post-treatment value, while in one out of four patients of the rigid contouring group the post-treatment NTL mean absorbed dose was higher than the pre-treatment one, probably due to a misalignment of the rigid image registration of a target with a volume of 2 mL. For this patient, nevertheless, no liver toxicity was reported after TARE treatment.

The CCCo among NTL mean absorbed doses (i.e., $D_{NTL,m}$ vs. $D_{NTL,r}$, $D_{NTL,m}$ vs.$D_{NTL,d}$ and $D_{NTL,r}$ vs. $D_{NTL,d}$) was 0.798 (0.710; 0.862), 0.755 (0.649; 0.832) and 0.926 (0.886; 0.953) for HCC/CCC patients and 0.913 (0.805; 0.962), 0.846 (0.632; 0.940) and 0.965 (0.889; 0.989) for metastatic patients.

3.4. Overall Survival and Mean Absorbed Doses

The Kaplan–Meier curves of overall survival according to the tumor type for the entire cohort of patients are reported in Figure 4a. The HCC, CCC or mixed HCC/CCC showed similar OS while metastases (i.e., "mets" in Figure 4a) were statistically significantly different; thus, they were excluded for the subsequent analysis. The remaining patients were grouped together and will be referred to as HCC/CCC patients. The Kaplan–Meier curves for the HCC/CCC patients are reported in Figure 4b–d according to the pre-TARE tumor mean absorbed dose for (a) manual, and post-TARE tumor mean absorbed dose with (b) rigid and (c) deformable registration approaches. Higher mean absorbed doses were statistically significantly associated to good prognosis irrespective of tumor type except for metastatic patients.

The best cutoffs of $D_{T,m}$, $D_{T,r}$ and $D_{T,d}$ were 110, 90 and 85 Gy, respectively. Confusion matrices (Figure 5) for HCC/CCC patients (having a similar survival) revealed that the mislabeled rates were 13%, 16% and 7% using each specific cutoff for the following comparison groups: $D_{T,m}$ vs. $D_{T,r}$, $D_{T,m}$ vs. $D_{T,d}$, $D_{T,r}$ vs. $D_{T,d}$, respectively. Accordingly, for the same comparison groups, the concordance of values above/below the specific group cutoff was 87%, 84% and 93%, respectively. This means that a pre-treatment dose higher than 110 Gy is a good predictor of a post-treatment dose higher than 90 Gy and 85 Gy for

the rigid and deformable registration, respectively; thus, a pre-treatment dose higher than 110 Gy can be used to predict higher survival.

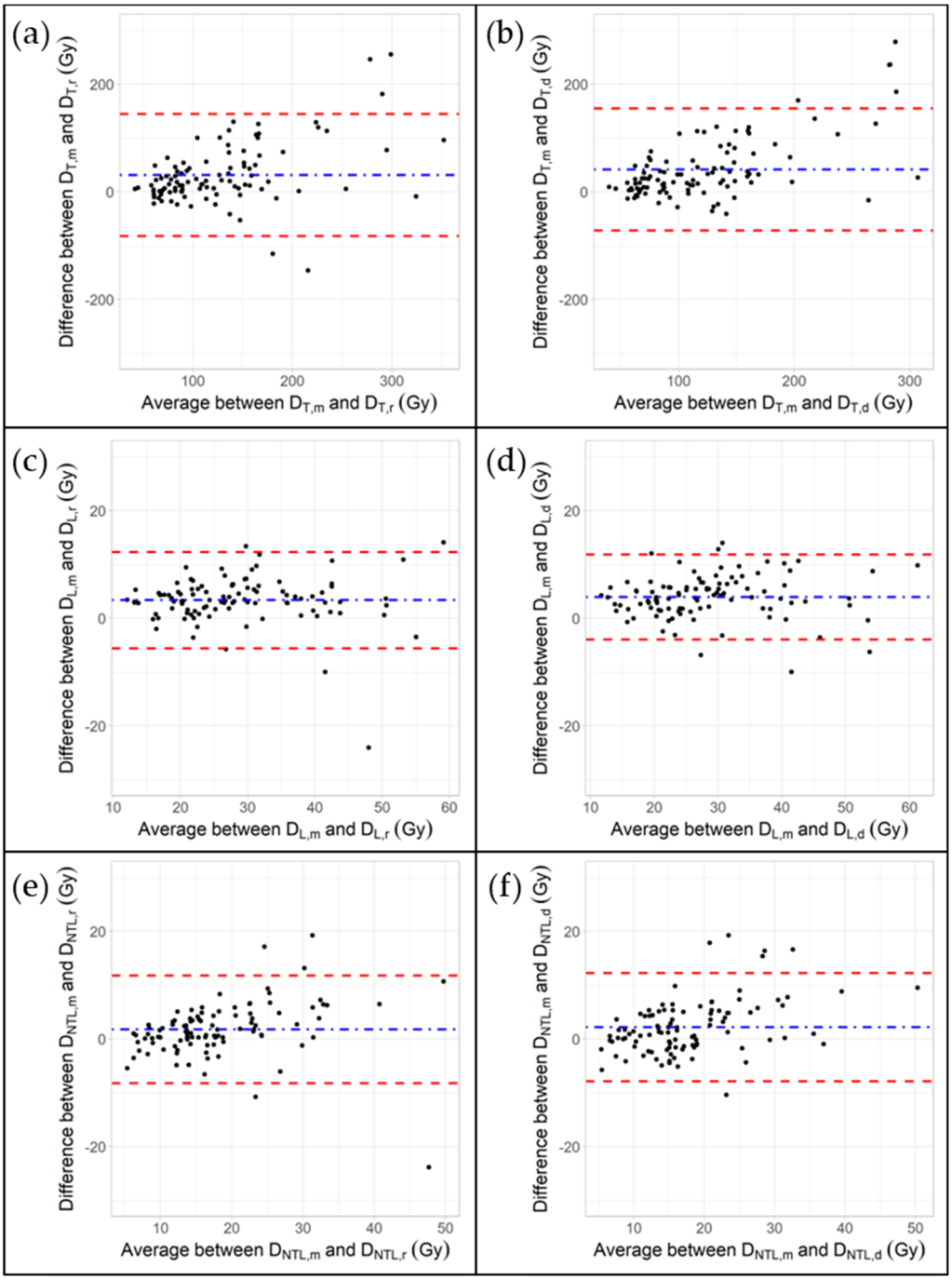

Figure 3. Bland–Altman plots for tumor (i.e., panels (**a**,**b**)), whole liver (i.e., panels (**c**,**d**)) and NTL (i.e., panels (**e**,**f**)) mean absorbed doses according to the contouring approach.

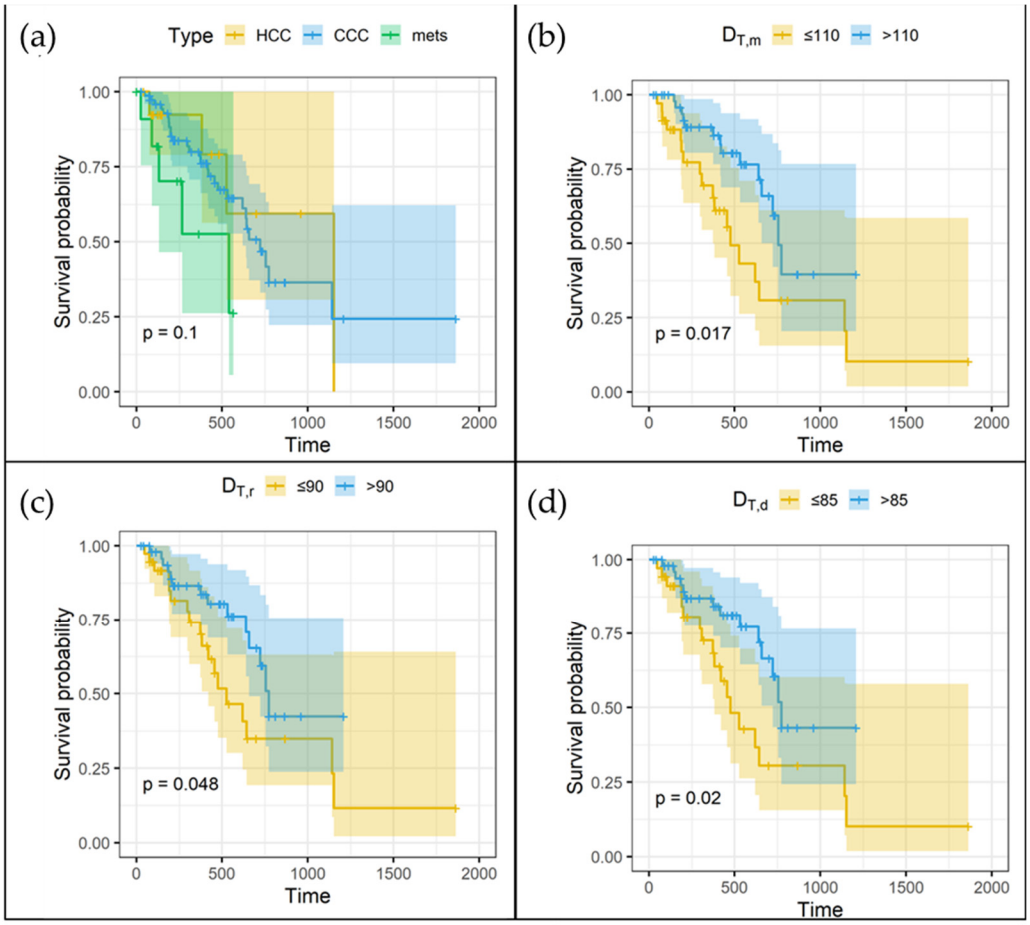

Figure 4. Kaplan–Meier curves of OS according to the (**a**) tumor type; K–M curves of OS for all HCC, CCC and mixed HCC/CCC patients according to the pre-TARE tumor mean absorbed dose for (**b**) manual, and post-TARE tumor mean absorbed dose with (**c**) rigid and (**d**) deformable registration approaches. Time is expressed in days.

(a)

	$D_{T,r}$≤90 Gy	$D_{T,r}$>90 Gy
$D_{T,m}$≤110 Gy	31 (35%)	5 (5%)
$D_{T,m}$>110 Gy	7 (8%)	46 (52%)

(b)

	$D_{T,d}$≤85 Gy	$D_{T,d}$>85 Gy
$D_{T,m}$≤110 Gy	29 (32%)	7 (8%)
$D_{T,m}$>110 Gy	7 (8%)	46 (52%)

(c)

	$D_{T,d}$≤85 Gy	$D_{T,d}$>85 Gy
$D_{T,r}$≤90 Gy	49 (55%)	4 (5%)
$D_{T,r}$>90 Gy	2 (2%)	34 (38%)

Figure 5. Confusion matrices for HCC/CCC patients for all the possible contouring comparisons: (**a**) manual and rigid; (**b**) manual and deformable; (**c**) rigid and deformable.

4. Discussion

In this study, we focused on the delineation of VOIs in primary and metastatic cancer patients undergoing cone beam CT-guided TARE treatment. In more detail, the impact of transferring manual VOIs to post-treatment images was investigated. Although a high correlation was suggested using each single modality, the pre-treatment and post-treatment volumes and mean absorbed doses in the tumor, liver and NTL showed several discrepancies as highlighted in the following discussion.

4.1. Bland–Altman Plots

The Bland–Altman analyses revealed that the deformable registration approach increased the volumes with regards to the manual one for all the delineated VOIs with a bias (LOA-; LOA+) of −25.6 mL (−115.3; 64.2), −103.4 mL (−403.4; 196.5), −76.5 mL (−349.1; 196.1) for tumor, liver and NTL, respectively. These differences might be due to the dependence of the deformable registration algorithms on liver shape and tumor displacement, which could be strongly affected by the differences in the respiratory phase during the CT acquisition. On the contrary, as expected, the rigid registration kept the volumes almost the same. The slight differences in volume values could be due to the rounding effect in the rototranslation of the VOIs and to the different slice thickness between the CT images of our SPECT/CT and PET/CT systems (i.e., 3.75 mm and 2.78 mm, respectively). Accordingly, the average increase in $V_{T,d}$ and $V_{NTL,d}$ with respect to $V_{T,m}$ and $V_{NTL,m}$ (i.e., a negative bias in Figure 2b) is mirrored by a decrease in the absorbed mean doses of these VOIs. On the contrary, although the volumes are maintained by the rigid registration, a reduction of the $D_{T,r}$ and $D_{NTL,r}$ (i.e., a positive bias in Figure 3a,e) is observed. This is likely to be ascribed to the mispositioning of the VOIs when shape and volume are constrained by the rigid algorithm.

For all the possible combinations in NTL mean absorbed dose (i.e., $D_{NTL,m}$ vs. $D_{NTL,r}$, $D_{NTL,m}$ vs. $D_{NTL,d}$ and $D_{NTL,r}$ vs. $D_{NTL,d}$), the Bland–Altman analyses resulted in a maximum bias of 2.3 Gy [−8.8;13.5]. These results were similar to the ones reported in Richetta et al. [15] for 10 HCC patients (i.e., 0.9 Gy (−7.4; 9.1)) using a manually adjusted delineation in both pre- and post-treatment images. On the contrary, tumor mean absorbed dose showed larger biases and LOAs for all the possible combinations (i.e., $D_{T,m}$ vs. $D_{T,r}$, $D_{T,m}$ vs.$D_{T,d}$ and $D_{T,r}$ vs.$D_{T,d}$ were 31.2 Gy (−80.6; 143.0), 41.7 Gy (−70.1; 153.5) and 10.5 Gy (−37.1; 58.1), respectively) when compared to the same study (i.e., −5.8 (−79.7; 68.2)). These discrepancies are likely due to the different range of evaluated tumor volumes between the two investigated populations and to the VOI delineation/propagation methods. In particular, in our study tumor volumes ranged from 1.3 to 1702.9 mL, while in Richetta et al. they went from 20 to 647 mL, and the VOIs delineated on SPECT/CT images were copied on PET/CT images and adjusted by applying a threshold method to reproduce the same volume values.

Moreover, Brosch et al. [26], using a rigid registration approach, reported that the mean difference for the NTL mean absorbed dose using ^{99m}Tc-MAA SPECT/CT and ^{90}Y PET/CT was 2.1 Gy (−1.2; 5.5), while the mean difference for the tumor was 7.2 Gy (−32.9; 47.3) in nine HCC patients (with volumes ranging from 16 to 1760 mL).

These results showed a concordance between pre-treatment and post-treatment dosimetry better than the one reported in our study. The larger absorbed dose discrepancies experienced in our results could be due to the higher number of patients and tumor/liver shape and size variability.

The Bland–Altman plots reported by Jadoul et al. [17] showed that the variations between predicted and effective doses were markedly higher in the tumors than in the NTL, especially in lesions with major uptake. The mean differences in tumors were −11.4 Gy (−68.4; 45.7) for HCC and −8.23 Gy (−68.9; 52.5) for metastatic patients, while in NTL they were 0.22 Gy (−6.02; 6.47) for HCC and −1.41 Gy (−11.9; 9.06) for metastatic patients. Again, these results were obtained in a smaller patient cohort (19 HCC and 20 liver metastases), with tumor volumes delineated on the three-phase injected CT and subsequently transposed on the ^{99m}Tc-MAA SPECT/CT and ^{90}Y PET/CT studies with a slight visual adaptation to compensate for the small imperfections of co-registration and volume variations. However, this readjustment operation might have positively affected the results reported in [17] when compared to ours. In addition, the volume of the injected liver was determined on functional images using thresholding of 1% of the maximum activity, while our propagation was based on the morphological images (i.e., CT images). Of note, the search of the actual liver volume through a threshold operation on functional

images could be distorted by blurring artifacts related to respiratory motion in both PET and SPECT images [9] and by different image resolutions.

The Bland–Altman plots in d'Abadie et al. [18] also demonstrated that in 95% of cases, NTL doses calculated with ^{90}Y imaging were 21.2% below and 20.6% above whole normal liver doses calculated with MAA imaging (0.788–1.206; 95% LOA of logarithmic differences), while tumor-absorbed doses calculated with ^{90}Y imaging were 74.6% below and up to 4.5 times above tumor-absorbed doses evaluated with MAA imaging (0.254–4.485; 95% LOA of logarithmic differences).

4.2. Concordance Correlation Coefficients

The CCCos among tumor mean absorbed doses for metastatic patients (i.e., 0.58 (0.10–0.84)) were similar to the ones reported by Jadoul et al. [17] (i.e., 0.52 (0.50; 0.53)), while for HCC/CCC patients CCCos (i.e., 0.60 (0.48; 0.70)) were lower (i.e., 0.82 (0.79; 0.84)). For NTL mean absorbed doses, CCCos resulted in 0.91 (0.80; 0.96) vs. 0.80 (0.76; 0.83) in metastatic patients and 0.80 (0.71; 0.86) vs. 0.94 (0.93; 0.95) in HCC/CCC patients.

The difference between the predicted and the observed doses of NTL generally did not exceed 12 Gy, with few exceptions, similarly to Jadoul et al. [17].

Based on these results, the D_{NTL} were accurately predicted with MAA imaging and could be used to optimize the activity planning using the voxel dosimetry. Similar results were obtained by d'Abadie et al. [18] but using the partition model.

In more detail, in a cohort of 66 patients d'Abadie et al. [18] delineated the target using the baseline contrast-enhanced MRI or CT scan: these images were fused with ^{99m}Tc-MAA SPECT and ^{90}Y PET using a rigid registration. The correlation between ^{99m}Tc-MAA- and ^{90}Y-based dosimetry NTL doses was very strong with a median absolute deviation of only 1.9 Gy, while for tumor-absorbed dose discrepancies were larger.

4.3. Dose–Survival Relationship

The number of studies reporting a relationship between response and tumor dose are increasing over time for patients treated with TARE. Specifically concerning ^{90}Y-loaded resin microspheres, a threshold of 100–120 Gy as a predictor of treatment response or OS has been identified by several studies [27]. In this context, therefore, the cutoff reported in the cohort of patients investigated in this study was in agreement with other authors [7,28–30].

In detail, Strigari et al. reported a significantly higher mean target-absorbed dose of 99 Gy in patients with complete or partial tumor response using ^{90}Y-bremsstrahlung SPECT [30]. Allimant et al. [28] reported a TD of 92 Gy for predicting the complete or partial tumor response. In a much smaller series, all patients who showed a response after resin microsphere treatment had received a tumor dose of at least 91 Gy [29].

Moreover, Nodari et al. [7] reported a cutoff in terms of the target mean absorbed dose of 115 and 98 Gy, using ^{99m}Tc-MAA SPECT/CT- and ^{90}Y PET/CT-based dosimetry, respectively, for predicting the OS.

Of note, the methodology proposed in this paper for the evaluation of the impact of VOI transfer can also be applied to images from TARE patients treated with ^{90}Y-loaded glass or ^{166}Ho-PLLA microspheres. It should be noted, nevertheless, that the cutoffs of mean absorbed dose used for stratifying survival curves reported in this study are only applicable to ^{90}Y-loaded resin microspheres as the tumor mean absorbed doses that are needed to treat the patients depend on the characteristics of the used device (e.g., the specific activity per microsphere, the dose rate, the heterogeneity of the absorbed dose distribution and the embolization capability) [31,32]. In particular, these characteristics led to reported threshold doses ranging from 205 Gy to 257 Gy for various tumor types treated with ^{90}Y-loaded glass microspheres [27] and 90 Gy for colorectal cancer metastasis treated with ^{166}Ho microspheres [33].

In addition, the role of ^{99m}Tc-MAA should be carefully considered when compared to ^{90}Y-loaded resin/glass microspheres, due to the intrinsic differences in terms of shape, size, size variability, density and number of injected particles [20]. Moreover, there are

differences in the image-based activity quantification when comparing the ^{99m}Tc-MAA SPECT/CT and ^{90}Y PET/CT activity distributions. Both issues could partially explain the disagreement between pre- and post-treatment absorbed dose distributions reported in this study. These limitations could be overcome in ^{166}Ho-loaded microsphere TARE, where a superior predictive value of ^{166}Ho scout dose for intrahepatic distribution with respect to ^{99m}Tc-MAA was reported [34]. Nevertheless, the replication of the angiographic procedure simulated with the ^{99m}Tc-MAA or ^{166}Ho scout dose during the treatment still plays a critical role for the pre- and post-treatment absorbed dose distribution agreement [35].

A limitation of this study is that the post-treatment dosimetry image is optimized according to 2020 Hou, indicating 4000 as the optimal beta value for dosimetric purposes. Nevertheless, the results of the impact of VOI propagation remain generally applicable to reconstructed images. Of note, in all the patients we used the same ^{99m}Tc MAA SPECT/CT acquisition and reconstruction protocol.

Another issue is that the VOI propagation algorithm previously validated in Calusi et al. [25] is only based on the CT images of both SPECT/CT and PET/CT. In particular, we recognize that the hybrid CT has a poor image quality when compared to CECT but it is still able to capture the mechanical deformation of the liver that occurs between SPECT/CT and PET/CT image acquisitions due to patient breathing and positioning. In addition, the CT-based image registration may represent an advantage because it is not dependent on the possible mismatch of the activity distributions between the ^{99m}Tc-MAA SPECT and ^{90}Y PET images.

Concerning the possible misalignment from SPECT or PET images and the attenuation correction maps due to respiratory motion during each multimodality image acquisition, this problem was also addressed by our group developing an ad hoc solution for SPECT/CT motion correction [36], while a commercial PET/CT motion correction solution was developed [37] but is not available in our Institute. For this reason, we preferred to not apply any motion correction in this study.

In this work, only the mean absorbed doses on tumors and organs were reported. Nevertheless, the mean absorbed dose approach may not be suitable for all tumors. For example, large tumors with relevant volumes of necrosis are associated to lower mean absorbed doses given the heterogeneity of the activity distributions but may respond to TARE due to high uptake in vital areas. In practice, the mean absorbed dose of vital tumor volumes is generally higher than the one of the entire tumor volumes, leading to a possible change in the absorbed dose thresholds reported from our OS-based analysis. Moreover, since these volumes are typically visible in CECT in terms of contrast media uptake but not in hybrid CT images, necrotic volumes might represent a critical issue in the use of automatic contouring or re-contouring tools. The impact of necrosis in the assessment of mean absorbed dose to the vital areas of the tumors will be addressed in future studies.

As for future improvements, several proposed solutions for compensating the respiratory motion in SPECT/CT [36,38,39] and PET/CT [37] images could improve the image recovery and enable a better agreement among corrected pre- and post-TARE images, thus potentially reducing the dosimetric disagreement among VOIs.

5. Conclusions

Delineation methods might be crucial for assessing dosimetry in patients undergoing TARE. The possibility of VOI transferring between imaging modalities allows sparing time for re-contouring compared to manual delineation especially in large cohorts. In our study, high concordance was found between VOIs manually delineated in ^{99m}Tc-MAA SPECT/CT pre-treatment images and semi-automatically transferred on ^{90}Y PET/CT post-treatment images with a rigid or deformable approach. On the contrary, mean absorbed doses obtained by the above-mentioned VOIs showed higher discrepancies.

Survival analyses highlighted different thresholds of mean absorbed doses for OS in HCC/CCC patients obtained when considering the manual delineation approach for pre-treatment and the rigid or deformable approaches for post-treatment images.

Finally, the application of semiautomatic strategies for VOI transfer should be applied carefully especially for small tumors, representing the most critical subgroup.

Supplementary Materials: The following supporting information can be downloaded at: https://www.mdpi.com/article/10.3390/app122412767/s1.

Author Contributions: Conceptualization, L.S.; methodology, G.D.G.; formal analysis, M.S.; investigation, L.S., M.S. and G.D.G.; data curation, G.P, A.C., C.M. and E.L.R.; writing—original draft preparation, L.S., G.D.G. and G.P.; writing—review and editing, M.S. and S.S.; supervision, L.S.; funding acquisition, L.S. All authors have read and agreed to the published version of the manuscript.

Funding: This study was partially supported by Associazione Italiana di Ricerca sul Cancro (AIRC) IG 20809 (2017) PI: L. Strigari.

Institutional Review Board Statement: The study was based on two populations. The first was included in a study approved by the Ethics Committee of IRCCS Azienda Ospedaliero-Universitaria di Bologna (Project identification code: 742/2019/disp/AoUBo and clinicaltrial.gov ID: NCT05227482), while the second comprised retrospective liver cancer and metastatic patients who underwent TARE treatment.

Informed Consent Statement: The study was conducted in accordance with the Declaration of Helsinki. All the subjects enrolled in the prospective clinical trial funded by AIRC and approved by the Ethics Committee of IRCCS Azienda Ospedaliero-Universitaria di Bologna (Project identification code: 742/2019/disp/AoUBo and clinicaltrial.gov ID: NCT05227482) gave their informed consent for inclusion before they participated in the study. For the remaining patients, ethics approval was not necessary as this study involved the use of retrospective de-identified data according to "Determinazione AIFA-20 Marzo 2008 (G.U. n. 76, 31-03-2008)".

Data Availability Statement: Data are available based on a reasonable request to the corresponding author.

Acknowledgments: The authors acknowledge the Associazione Italiana di Ricerca sul Cancro (AIRC) partially supporting the study.

Conflicts of Interest: The authors declare no conflict of interest.

References

1. Levillain, H.; Bagni, O.; Deroose, C.M.; Dieudonné, A.; Gnesin, S.; Grosser, O.S.; Kappadath, S.C.; Kennedy, A.; Kokabi, N.; Liu, D.M.; et al. International recommendations for personalised selective internal radiation therapy of primary and metastatic liver diseases with yttrium-90 resin microspheres. *Eur. J. Nucl. Med. Mol. Imaging* **2021**, *48*, 1570–1584. [CrossRef] [PubMed]
2. Weber, M.; Lam, M.; Chiesa, C.; Konijnenberg, M.; Cremonesi, M.; Flamen, P.; Gnesin, S.; Bodei, L.; Kracmerova, T.; Luster, M.; et al. EANM procedure guideline for the treatment of liver cancer and liver metastases with intra-arterial radioactive compounds. *Eur. J. Nucl. Med. Mol. Imaging* **2022**, *49*, 1682–1699. [CrossRef] [PubMed]
3. Salem, R.; Padia, S.A.; Lam, M.; Bell, J.; Chiesa, C.; Fowers, K.; Hamilton, B.; Herman, J.; Kappadath, S.C.; Leung, T.; et al. Clinical and dosimetric considerations for Y90: Recommendations from an international multidisciplinary working group. *Eur. J. Nucl. Med. Mol. Imaging* **2019**, *46*, 1695–1704. [CrossRef] [PubMed]
4. Cremonesi, M.; Chiesa, C.; Strigari, L.; Ferrari, M.; Botta, F.; Guerriero, F.; De Cicco, C.; Bonomo, G.; Orsi, F.; Bodei, L.; et al. Radioembolization of hepatic lesions from a radiobiology and dosimetric perspective. *Front. Oncol.* **2014**, *4*, 210. [CrossRef]
5. Braat, A.J.A.T.; Prince, J.F.; van Rooij, R.; Bruijnen, R.C.G.; van den Bosch, M.A.A.J.; Lam, M.G.E.H. Safety analysis of holmium-166 microsphere scout dose imaging during radioembolisation work-up: A cohort study. *Eur. Radiol.* **2018**, *28*, 920–928. [CrossRef]
6. Della Gala, G.; Bardiès, M.; Tipping, J.; Strigari, L. Overview of commercial treatment planning systems for targeted radionuclide therapy. *Phys. Med.* **2021**, *92*, 52–61. [CrossRef]
7. Nodari, G.; Popoff, R.; Riedinger, J.M.; Lopez, O.; Pellegrinelli, J.; Dygai-Cochet, I.; Tabouret-Viaud, C.; Presles, B.; Chevallier, O.; Gehin, S.; et al. Impact of contouring methods on pre-treatment and post-treatment dosimetry for the prediction of tumor control and survival in HCC patients treated with selective internal radiation therapy. *EJNMMI Res.* **2021**, *11*, 24. [CrossRef]
8. Meyers, N.; Jadoul, A.; Bernard, C.; Delwaide, J.; Lamproye, A.; Detry, O.; Honoré, P.; Gerard, L.; Hustinx, R. Inter-observer variability of (90)Y PET/CT dosimetry in hepatocellular carcinoma after glass microspheres transarterial radioembolization. *EJNMMI Phys.* **2020**, *7*, 29. [CrossRef]
9. Kyme, A.Z.; Fulton, R.R. Motion estimation and correction in SPECT, PET and CT. *Phys. Med. Biol.* **2021**, *66*, 18TR02. [CrossRef]
10. Morán, V.; Prieto, E.; Sancho, L.; Rodríguez-Fraile, M.; Soria, L.; Zubiria, A.; Martí-Climent, J.M. Impact of the dosimetry approach on the resulting (90)Y radioembolization planned absorbed doses based on (99m)Tc-MAA SPECT-CT: Is there agreement between dosimetry methods? *EJNMMI Phys.* **2020**, *7*, 72. [CrossRef]

11. Pasciak, A.S.; Erwin, W.D. Effect of voxel size and computation method on Tc-99m MAA SPECT/CT-based dose estimation for Y-90 microsphere therapy. *IEEE Trans. Med. Imaging* **2009**, *28*, 1754–1758. [CrossRef]
12. D'Arienzo, M.; Pimpinella, M.; Capogni, M.; De Coste, V.; Filippi, L.; Spezi, E.; Patterson, N.; Mariotti, F.; Ferrari, P.; Chiaramida, P.; et al. Phantom validation of quantitative Y-90 PET/CT-based dosimetry in liver radioembolization. *EJNMMI Res.* **2017**, *7*, 94. [CrossRef] [PubMed]
13. Knešaurek, K. Comparison of posttherapy (90)Y positron emission tomography/computed tomography dosimetry methods in liver therapy with (90)Y microspheres. *World J. Nucl. Med.* **2020**, *19*, 359–365. [CrossRef]
14. Hermann, A.L.; Dieudonné, A.; Ronot, M.; Sanchez, M.; Pereira, H.; Chatellier, G.; Garin, E.; Castera, L.; Lebtahi, R.; Vilgrain, V. Relationship of Tumor Radiation-absorbed Dose to Survival and Response in Hepatocellular Carcinoma Treated with Transarterial Radioembolization with (90)Y in the SARAH Study. *Radiology* **2020**, *296*, 673–684. [CrossRef] [PubMed]
15. Richetta, E.; Pasquino, M.; Poli, M.; Cutaia, C.; Valero, C.; Tabone, M.; Paradisi, B.P.; Pacilio, M.; Pellerito, R.E.; Stasi, M. PET-CT post therapy dosimetry in radioembolization with resin (90)Y microspheres: Comparison with pre-treatment SPECT-CT (99m)Tc-MAA results. *Phys. Med.* **2019**, *64*, 16–23. [CrossRef] [PubMed]
16. Kafrouni, M.; Allimant, C.; Fourcade, M.; Vauclin, S.; Guiu, B.; Mariano-Goulart, D.; Ben Bouallègue, F. Analysis of differences between (99m)Tc-MAA SPECT- and (90)Y-microsphere PET-based dosimetry for hepatocellular carcinoma selective internal radiation therapy. *EJNMMI Res.* **2019**, *9*, 62. [CrossRef]
17. Jadoul, A.; Bernard, C.; Lovinfosse, P.; Gérard, L.; Lilet, H.; Cornet, O.; Hustinx, R. Comparative dosimetry between (99m)Tc-MAA SPECT/CT and (90)Y PET/CT in primary and metastatic liver tumors. *Eur. J. Nucl. Med. Mol. Imaging* **2020**, *47*, 828–837. [CrossRef]
18. d'Abadie, P.; Walrand, S.; Hesse, M.; Amini, N.; Lhommel, R.; Sawadogo, K.; Jamar, F. Accurate non-tumoral 99mTc-MAA absorbed dose prediction to plan optimized activities in liver radioembolization using resin microspheres. *Phys. Med.* **2021**, *89*, 250–257. [CrossRef]
19. Gramenzi, A.; Golfieri, R.; Mosconi, C.; Cappelli, A.; Granito, A.; Cucchetti, A.; Marinelli, S.; Pettinato, C.; Erroi, V.; Fiumana, S.; et al. Yttrium-90 radioembolization vs sorafenib for intermediate-locally advanced hepatocellular carcinoma: A cohort study with propensity score analysis. *Liver Int.* **2015**, *35*, 1036–1047. [CrossRef]
20. Kim, S.P.; Cohalan, C.; Kopek, N.; Enger, S.A. A guide to (90)Y radioembolization and its dosimetry. *Phys. Med.* **2019**, *68*, 132–145. [CrossRef]
21. Ahmadzadehfar, H.; Haslerud, T.; Reichmann, K.; Meyer, C.; Habibi, E.; Fimmers, R.; Muckle, M.; Sabet, A.; Biersack, H.J.; Ezziddin, S. Residual activity after radioembolization of liver tumours with 90Y resin microspheres. A safe calculation method. *Nuklearmedizin* **2014**, *53*, 95–98. [CrossRef] [PubMed]
22. Available online: https://www.gehealthcare.com/en-sg/-/jssmedia/widen/2018/01/25/0204/gehealthcarecom/migrated/2018/03/22/0155/ocuments-us-global-products-pet-ct-whitepaper-q-clear-ge-healthcare-white-paper_qclear_pdf.pdf?rev=-1 (accessed on 30 November 2022).
23. Rowley, L.M.; Bradley, K.M.; Boardman, P.; Hallam, A.; McGowan, D.R. Optimization of Image Reconstruction for (90)Y Selective Internal Radiotherapy on a Lutetium Yttrium Orthosilicate PET/CT System Using a Bayesian Penalized Likelihood Reconstruction Algorithm. *J. Nucl. Med.* **2017**, *58*, 658–664. [CrossRef] [PubMed]
24. Hou, X.; Ma, H.; Esquinas, P.L.; Uribe, C.F.; Tolhurst, S.; Bénard, F.; Liu, D.; Rahmim, A.; Celler, A. Impact of image reconstruction method on dose distributions derived from(90)Y PET images: Phantom and liver radioembolization patient studies. *Phys. Med. Biol.* **2020**, *65*, 215022. [CrossRef]
25. Calusi, S.; Labanca, G.; Zani, M.; Casati, M.; Marrazzo, L.; Noferini, L.; Talamonti, C.; Fusi, F.; Desideri, I.; Bonomo, P.; et al. A multiparametric method to assess the MIM deformable image registration algorithm. *J. Appl. Clin. Med. Phys.* **2019**, *20*, 75–82. [CrossRef]
26. Brosch, J.; Gosewisch, A.; Kaiser, L.; Seidensticker, M.; Ricke, J.; Zellmer, J.; Bartenstein, P.; Ziegler, S.; Ilhan, H.; Todica, A.; et al. 3D image-based dosimetry for Yttrium-90 radioembolization of hepatocellular carcinoma: Impact of imaging method on absorbed dose estimates. *Phys. Med.* **2020**, *80*, 317–326. [CrossRef] [PubMed]
27. Garin, E.; Rolland, Y.; Edeline, J. (90)Y-Loaded Microsphere SIRT of HCC Patients with Portal Vein Thrombosis: High Clinical Impact of 99mTc-MAA SPECT/CT-Based Dosimetry. *Semin. Nucl. Med.* **2019**, *49*, 218–226. [CrossRef] [PubMed]
28. Allimant, C.; Kafrouni, M.; Delicque, J.; Ilonca, D.; Cassinotto, C.; Assenat, E.; Ursic-Bedoya, J.; Pageaux, G.P.; Mariano-Goulart, D.; Aho, S.; et al. Tumor Targeting and Three-Dimensional Voxel-Based Dosimetry to Predict Tumor Response, Toxicity, and Survival after Yttrium-90 Resin Microsphere Radioembolization in Hepatocellular Carcinoma. *J. Vasc. Interv. Radiol.* **2018**, *29*, 1662–1670.e4. [CrossRef]
29. Kao, Y.H.; Steinberg, J.D.; Tay, Y.S.; Lim, G.K.; Yan, J.; Townsend, D.W.; Budgeon, C.A.; Boucek, J.A.; Francis, R.J.; Cheo, T.S.; et al. Post-radioembolization yttrium-90 PET/CT—Part 2: Dose-response and tumor predictive dosimetry for resin microspheres. *EJNMMI Res.* **2013**, *3*, 57. [CrossRef] [PubMed]
30. Strigari, L.; Sciuto, R.; Rea, S.; Carpanese, L.; Pizzi, G.; Soriani, A.; Iaccarino, G.; Benassi, M.; Ettorre, G.M.; Maini, C.L. Efficacy and toxicity related to treatment of hepatocellular carcinoma with 90Y-SIR spheres: Radiobiologic considerations. *J. Nucl. Med.* **2010**, *51*, 1377–1385. [CrossRef] [PubMed]
31. Garin, E.; Guiu, B.; Edeline, J.; Rolland, Y.; Palard, X. Trans-arterial Radioembolization Dosimetry in 2022. *CardioVasc. Interv. Radiol.* **2022**, *45*, 1608–1621. [CrossRef]

32. Walrand, S.; Hesse, M.; Chiesa, C.; Lhommel, R.; Jamar, F. The low hepatic toxicity per Gray of 90Y glass microspheres is linked to their transport in the arterial tree favoring a nonuniform trapping as observed in posttherapy PET imaging. *J. Nucl. Med.* **2014**, *55*, 135–140. [CrossRef]
33. van Roekel, C.; Bastiaannet, R.; Smits, M.L.J.; Bruijnen, R.C.; Braat, A.; de Jong, H.; Elias, S.G.; Lam, M. Dose-Effect Relationships of (166)Ho Radioembolization in Colorectal Cancer. *J. Nucl. Med.* **2021**, *62*, 272–279. [CrossRef] [PubMed]
34. Smits, M.L.J.; Dassen, M.G.; Prince, J.F.; Braat, A.; Beijst, C.; Bruijnen, R.C.G.; de Jong, H.; Lam, M. The superior predictive value of (166)Ho-scout compared with (99m)Tc-macroaggregated albumin prior to (166)Ho-microspheres radioembolization in patients with liver metastases. *Eur. J. Nucl. Med. Mol. Imaging* **2020**, *47*, 798–806. [CrossRef] [PubMed]
35. Thomas, M.A.; Mahvash, A.; Abdelsalam, M.; Kaseb, A.O.; Kappadath, S.C. Planning dosimetry for (90) Y radioembolization with glass microspheres: Evaluating the fidelity of (99m) Tc-MAA and partition model predictions. *Med. Phys.* **2020**, *47*, 5333–5342. [CrossRef] [PubMed]
36. Santoro, M.; Della Gala, G.; Paolani, G.; Zagni, F.; Strolin, S.; Civollani, S.; Calderoni, L.; Cappelli, A.; Mosconi, C.; Lodi Rizzini, E.; et al. A novel tool for motion-related dose inaccuracies reduction in (99m)Tc-MAA SPECT/CT images for SIRT planning. *Phys. Med.* **2022**, *98*, 98–112. [CrossRef]
37. van der Vos, C.S.; Koopman, D.; Rijnsdorp, S.; Arends, A.J.; Boellaard, R.; van Dalen, J.A.; Lubberink, M.; Willemsen, A.T.M.; Visser, E.P. Quantification, improvement, and harmonization of small lesion detection with state-of-the-art PET. *Eur. J. Nucl. Med. Mol. Imaging* **2017**, *44*, 4–16. [CrossRef]
38. Sanders, J.C.; Ritt, P.; Kuwert, T.; Vija, A.H.; Maier, A.K. Fully Automated Data-Driven Respiratory Signal Extraction from SPECT Images Using Laplacian Eigenmaps. *IEEE Trans. Med. Imaging* **2016**, *35*, 2425–2435. [CrossRef]
39. Robert, A.; Rit, S.; Baudier, T.; Jomier, J.; Sarrut, D. Data-Driven Respiration-Gated SPECT for Liver Radioembolization. *IEEE Trans. Radiat. Plasma Med. Sci.* **2022**, *6*, 778–787. [CrossRef]